Two-phase damping and interface surface area in tubes with vertical internal flow ☆

C. Béguin, F. Anscutter, A. Ross*, M.J. Pettigrew, N.W. Mureithi

Department of Mechanical Engineering, École Polytechnique, P.O. Box 6079, succ. Centre-Ville, Montréal, Que., Canada H3C 3A7

Abstract

Two-phase flow is common in the nuclear industry. It is a potential source of vibration in piping systems. In this paper, two-phase damping in the bubbly flow regime is related to the interface surface area and, therefore, to flow configuration. Experiments were performed with a vertical tube clamped at both ends. First, gas bubbles of controlled geometry were simulated with glass spheres let to settle in stagnant water. Second, air was injected in stagnant alcohol to generate a uniform and measurable bubble flow. In both cases, the two-phase damping ratio is correlated to the number of bubbles (or spheres). Two-phase damping is directly related to the interface surface area, based on a spherical bubble model. Further experiments were carried out on tubes with internal two-phase air–water flows. A strong dependence of two-phase damping on flow parameters in the bubbly flow regime is observed. A series of photographs attests to the fact that two-phase damping in bubbly flow increases for a larger number of bubbles, and for smaller bubbles. It is highest immediately prior to the transition from bubbly flow to slug or churn flow regimes. Beyond the transition, damping decreases. It is also shown that two-phase damping increases with the tube diameter.
© 2008 Elsevier Ltd. All rights reserved.

Keywords: Internal two-phase flow; Two-phase damping; Flow regime; Interface surface area; Tube diameter

1. Introduction

In the nuclear industry, heat exchangers and piping elements are often subjected to two-phase flows. Flow-induced vibration can lead to structural degradation, process malfunction, and component failure. Two-phase damping can significantly contribute to reducing vibration and thus, to prevent premature fatigue or wear. Therefore, it is desirable to identify some of the parameters that govern two-phase damping in pipes with internal two-phase flow. In the present paper, we propose to correlate two-phase damping with the interface surface area.

The first damping experiments on a tube subjected to two-phase flow were performed some 25 years ago. Carlucci (1980) carried out a series of tests on tubes subjected to an axially confined air–water two-phase flow. His results showed that damping in two-phase flow strongly depends on void fraction, but no significant relation was found with fluid mixture velocity. Many researchers have since contributed to the knowledge of two-phase damping. Recently,

Nomenclature

A	surface area (m^2)	W	mass flow rate (kg/s)
B_i	various constants	X	lateral bubble position inside tube (m)
b_i	integration constants	Y	lateral tube displacement (m)
c	damping coefficient (N s/m)	U	superficial velocity (m/s)
d	bubble diameter (mm)	V	volume of fluid (m^3)
D	tube diameter (mm)	β	volumetric quality
E	Young's modulus (GPa)	ΔL	unit length of tube (m)
E_γ	surface energy (J)	γ	surface tension (N/m)
E_{damp}	energy dissipated by damping (J)	ε	void fraction
F	force (N)	ζ	damping ratio (%)
f_n	natural frequency (Hz)	μ	viscosity (Pa s)
f	friction factor	v	kinematic viscosity (m^2/s)
g	gravitational acceleration (m/s^2)	ρ	mass density (kg/m^3)
I	tube second moment of area (mm^4)	τ	power dissipation per unit mass in turbulent pipe flow (W/kg)
I_i, K_i	modified Bessel function		
k	stiffness (N/m)	*Subscripts*	
l	inter-bubble distance (m)	b	bubble, or sphere
L	tube length (m)	o	outer
m	mass per unit length (kg/m)	f	flow-dependent
M	reduced mass	g	gas
N	number of bubbles per unit length of tube	i	inner
P	fluid pressure (Pa)	l	liquid
Q	volume flow rate (m^3/s)	s	structural
r, θ	cylindrical coordinate	v	viscous
S	interface surface area (m^2)	t	total
S_r	slip ratio between phases	2φ	two-phase
U_R	reduced velocity		

Gravelle et al. (2007) shed new light on the parameters that govern two-phase damping in vertical tubes with internal air–water two-phase flows. The experiments showed that damping is affected by void fraction, flow velocity, and flow regime. The authors suggested that the interface surface area, which depends on the flow regime, may be a dominant factor. This paper is intended to prove the validity of this hypothesis by means of simple experiments. In addition, tube diameter is also investigated as an important parameter affecting damping.

2. Two-phase flow considerations

2.1. Basic definitions

The proportion of gas in a two-phase gas–liquid mixture is characterized either by the void fraction ε or by the volumetric quality β (Collier and Thome, 1996). In one unit length ΔL of a two-phase mixture inside a tube, void fraction and volumetric quality are defined as

$$\varepsilon = \frac{V_g}{V_g + V_l} = \frac{A_g \Delta L}{A_g \Delta L + A_l \Delta L} = \frac{A_g}{A_g + A_l} \tag{1}$$

and

$$\beta = \frac{Q_g}{Q_g + Q_l} = \frac{A_g \Delta L\, U_g}{A_g \Delta L\, U_g + A_l \Delta L\, U_l} = \frac{A_g}{A_g + A_l(U_l/U_g)} = \frac{A_g}{A_g + A_l S_r}, \tag{2}$$

where V_g and V_l are the volumes of the gas and liquid phases in the mixture, A_g and A_l are the areas of each phase in the tube section, Q_g and Q_l are the volume flow rates, U_g and U_l are the velocities of each phase. Each proportion is related to the other through the slip ratio between phases, $S_r = U_g /U_l$.

2.2. Damping in two-phase flow

When a single-phase fluid flows through a transversely vibrating tube, the transverse motion $x(\xi,t)$ of the tube can be damped by the fluid motion (ξ is the axial position along the tube and t is the time). The equation of motion of such system is as follows (de Langre, 2002):

$$(MU_R^2 - 1)\frac{\partial^2 x}{\partial \xi^2} + 2MU_R\frac{\partial^2 x}{\partial \xi \partial t} + (M+1)\frac{\partial^2 x}{\partial t^2} = 0. \tag{3}$$

The dimensionless mass of the fluid is given by $M = \rho A/m$, where m is the mass per unit length of the tube. The reduced velocity of the fluid is given using the velocity of the transverse wave in the tube itself: $U_R = U/(T/m)^{1/2}$, where T is the tension in the tube.

In the second term of Eq. (3), the axial velocity U_R of the fluid mass inside the transversely vibrating tube causes a Coriolis type force due to the rotation $\partial x/\partial \xi$ of the tube. This force is proportional to the transverse velocity $\partial x/\partial t$ of the tube: it thus acts as a damping element on the tube. It can be shown from Eq. (3) that for low flow velocities, flow-dependent damping is positive: the vibration of the tube is reduced and kinetic energy is either transferred to the fluid flow or dissipated (de Langre, 2002).

Carlucci (1980) have reported that damping in two-phase flows is much greater than it is in single-phase flows. Thus, the concept of two-phase damping was introduced to allow for this difference. Damping in two-phase flows therefore includes the following components: (i) ζ_s: structural damping; (ii) ζ_v: viscous damping; (iii) ζ_f: flow-dependent damping; and (iv) $\zeta_{2\varphi}$: two-phase damping.

Fig. 1 shows the contribution of each component to the total damping ratio for confined annular air–water axial flow. Structural damping depends on the tube material and supports; it is not shown in this figure. Two-phase damping $\zeta_{2\varphi}$ is preponderant and strongly depends on void fraction. Carlucci and Brown (1983) suggested that the Coriolis force in Eq. (3) should be written as

$$2MU_R\frac{\partial^2 x}{\partial \xi \partial t} + \underbrace{\left(\frac{\partial M}{\partial t} + U_R\frac{\partial M}{\partial \xi}\right)\frac{\partial x}{\partial t}}_{\text{Two-phase random Coriolis}}.$$
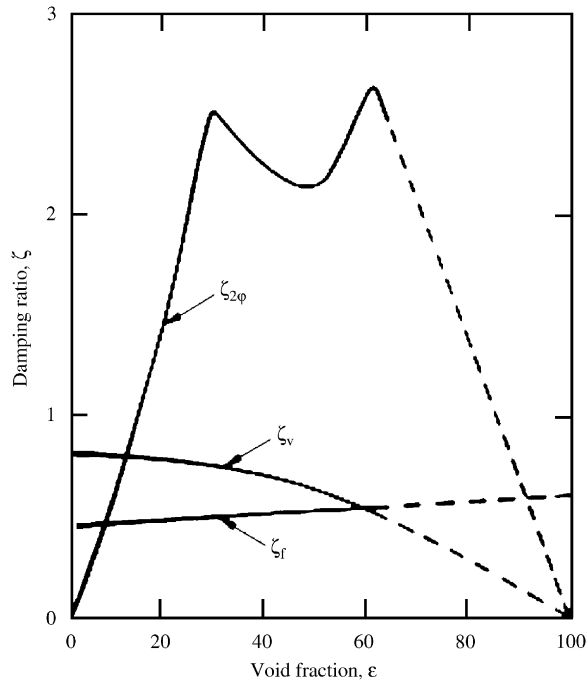

Fig. 1. Components of total damping in two-phase flow (Carlucci, 1980).

This effect causes a detuning mechanism that could explain two-phase damping, but this model does not explain dependency on void fraction. Hara and Kohgo (1985) considered a bubbly flow forced to oscillate due to a vibrating structure. In this model, the motion of bubbles in the liquid is governed by added mass and fluid viscosity. The energy dissipation is due to the liquid viscosity acting between the vibrating gas columns and liquid. Although Carlucci's and Hara's tests were performed with an axially confined external flow, the various damping mechanisms in an internal flow are expected to be the same. The geometric configuration is different, but the motion of the tube and the dependence of two-phase damping on void fraction should exhibit similar trends.

Carlucci and Brown (1983) suggested that the total damping ratio ζ_s should be given by the sum of the various damping components:

$$\zeta_t = \zeta_s + \zeta_v + \zeta_f + \zeta_{2\varphi}. \tag{4}$$

Carlucci found two-phase damping to be a dominant component in the 30–80% void fraction range, as in Fig. 1. However, in the tests described hereafter, we found that the viscous component ζ_v and the flow-dependent component ζ_f were small with respect to the two-phase component $\zeta_{2\varphi}$ over the entire range of void fractions. ζ_s was measured with stagnant water and stagnant air. Total damping was measured at 0% and 100% void fractions (where $\zeta_{2\varphi} = 0$), for various flow velocities. For each condition, the difference between total damping and structural damping was not significant; thus, the sum of viscous and flow-dependent damping was found to be negligible in our single-phase experiments, at the flow rates considered. Fig. 1 shows that both viscous and flow-dependent components are monotonic functions of void fraction. Therefore, these two components (ζ_v and ζ_f) were considered to be negligible for all void fractions from 0% to 100%.

Finally, the measured structural damping ratio ζ_s ranges between 0.6% and 0.7%, which is much less than the two-phase damping ratios reported in the following sections, hence $\zeta_v + \zeta_f \ll \zeta_s < \zeta_{2\varphi}$.

Thus, viscous damping and flow-dependent damping were ignored and the two-phase component $\zeta_{2\varphi}$ was calculated as

$$\zeta_{2\varphi} = \zeta_t - \zeta_s. \tag{5}$$

2.3. Two-phase flow regimes

Two-phase flow analysis is formulated from the classical fluid mechanics conservation law. Our discussion will be focused on the homogeneous flow model. In this model, the two-phase mixture is considered as a single fluid whose physical properties correspond to the averaged properties of the phases (Wallis, 1969). The homogeneous model assumes that velocity is the same for both phases, so $S_r = 1$ and $\varepsilon = \beta$.

In two-phase flow, the configuration of the deformable interface between phases is of critical importance to determine mixture properties. Each phase interacts with the tube wall through friction forces, and with the other phase through interfacial forces. The flow structure in gas–liquid vertical flow is commonly categorized into the following flow regimes:

(a) *Bubbly flow*: At low flow rates, the gas phase is dispersed in relatively large deformable bubbles.
(b) *Finely dispersed bubble flow*: By increasing the liquid flow rate, the large bubbles break up due to turbulence. The small bubbles disperse in the liquid, and coalescence is inhibited by the turbulence.
(c) *Slug flow*: By increasing the gas flow rate, bubbles agglomerate. Part of the gas phase is arranged in bubbly water slugs and Taylor bubbles. The photographs in Fig. 2 show the transition from bubbly to slug flow for a given flow velocity when the void fraction is increased from 6% to 22%.
(d) *Churn flow*: Churn flow is similar to slug flow. When the gas flow rate of slug flow is increased, slugs become smaller, distorted, and unstable. The flow is more random. Some authors report that slug/churn flow transition is not easy to discern, and instead introduce stable and unstable slug flows (Costigan and Whalley, 1997). For the sake of simplicity in this paper, both slug and churn flow regimes are referred to as the slug/churn regime.
(e) *Annular flow*: At high gas flow rates, the liquid phase forms a layer along the tube wall. The gas fills the centre of the tube.

3. Two-phase damping mechanism in bubbly flow

The proposed flow pattern identification technique is based on previous observations according to which two-phase damping is maximum at void fractions immediately below the transition from bubbly to slug/churn flow (Gravelle et al., 2007). As shown below, the surface energy variations of the bubbles do not contribute significantly to two-phase
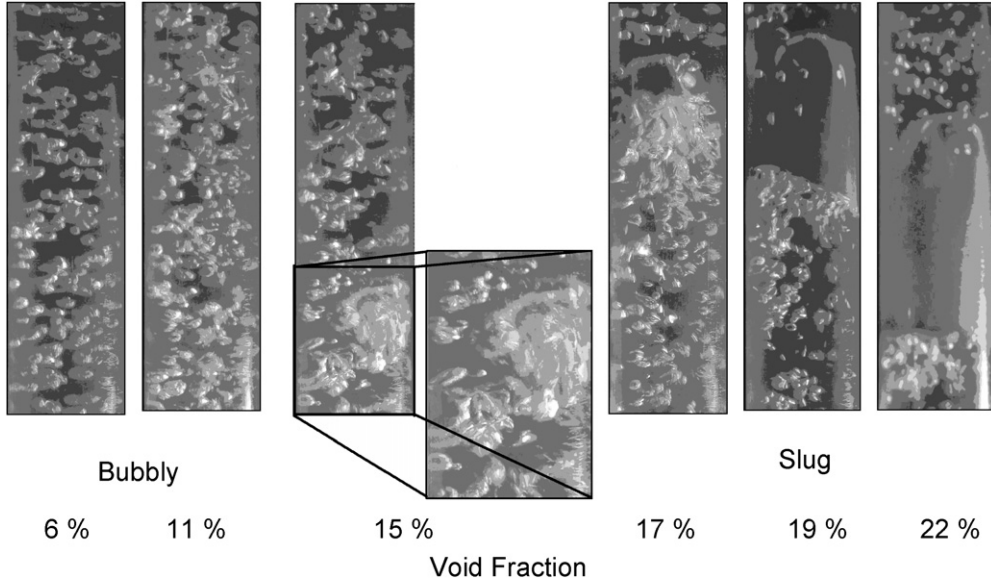
Fig. 2. Illustration of transition between bubbly flow and slug flow.

damping. In bubbly flow, it is proposed that viscous dissipation is responsible for two-phase damping, and that it is proportional to the interface surface area.

3.1. Estimate of surface energy dissipation

The interface surface area is written as

$$S = \sum_{k=1}^{N} S_{b,k} = \sum_{k=1}^{N} \pi d_{b,k}^2 = N\pi\langle d_b^2\rangle, \tag{6}$$

where $S_{b,k}$ and $d_{b,k}$ are the surface area and diameter of the kth bubble, $\langle d_b^2\rangle$ is the average squared diameter of the bubbles, and N is the number of bubbles. In addition,

$$N = \frac{V_g}{\langle V_b\rangle} = \frac{\varepsilon\pi(D_i/2)^2 L}{(\pi/6)\langle d_b^3\rangle}. \tag{7}$$

So,

$$S = \frac{3\pi\varepsilon D_i^2 L\langle d_b^2\rangle}{2\langle d_b^3\rangle}, \tag{8}$$

where L and D_i are the length and inside diameter of the tube. Riverin and Pettigrew (2004) suggested that bubble diameters follow a Rayleigh distribution in this case:

$$\frac{\langle d_b^2\rangle}{\langle d_b^3\rangle} = \frac{B_1}{\langle d_b\rangle} = \frac{B_2}{d_{max}}, \tag{9}$$

where B_1 and B_2 are constants and d_{max} is the maximum bubble diameter. The surface energy is related to the surface tension γ:

$$E_\gamma = \gamma S = \frac{\gamma 3\pi\varepsilon B_2 D_i^2 L}{2 d_{max}}. \tag{10}$$

The bubble diameter suggested by Hinze (1955) for a bubbly flow is

$$d_{max} = 1.14 \left(\frac{\gamma}{\rho_l} \right)^{3/5} \tau^{-2/5}, \tag{11}$$

where the power dissipation per unit mass in turbulent pipe flow, τ, is given as (Taitel et al., 1980)

$$\tau = \left| \frac{\partial P}{\partial L} \right| \frac{U_{2\varphi}}{\rho_{2\varphi}} = \left| \frac{2f}{D_i} \rho_{2\varphi} U_{2\varphi}^2 \right| \frac{U_{2\varphi}}{\rho_{2\varphi}}, \tag{12}$$

where $U_{2\varphi}$ and $\rho_{2\varphi}$ are the homogeneous velocity and density of the two-phase flow, and P is the pressure in the fluid. The friction factor f is (Hinze, 1955):

$$f = 0.046 \left(\frac{U_{2\varphi} D_i}{v_l} \right)^{-1/5}. \tag{13}$$

Finally, from Eqs. (9)–(12), the maximum surface energy in a 1 m long bubbly air–water flow can be estimated:

$$E_\gamma = \gamma S = 1.6 B_2 \gamma^{0.4} \rho_L^{0.6} U_{2\varphi}^{1.12} D_i^{1.52} v_L^{0.08} \varepsilon, \tag{14}$$

where

$$B_2 = \frac{d_{max} \langle d_b^2 \rangle}{\langle d_b^3 \rangle}. $$

It should be noted that

(a) Bubbly flow is the pattern having the greatest surface energy.
(b) By choosing conservative values $B_2 = 2$, $\gamma = 0.076 \, \text{N/m}^2$, $\rho_l = 1000 \, \text{kg/m}^3$, $v_l = 10^{-6} \, \text{m}^2/\text{s}$, $U_{2\varphi} < 5 \, \text{m/s}$, $D_i = 0.021 \, \text{m}$ and $\varepsilon < 1$ the maximum surface energy in bubbly flow is estimated to be $E_\gamma < 0.38 \, \text{J}$. It should be noted that based on a Rayleigh distribution of the bubble diameter, and defining d_{max} as the 99th percentile, parameter B_2 should not exceed 1.61; thus, $B_2 = 2$ is a conservative value.

We conclude that E_γ is certainly less than to 0.4 J in all cases. As shown below, this value is equivalent to the energy dissipated in one second by the free vibration of the tube with a 0.2% damping ratio. The equivalent stiffness, $k_t = 2660 \, \text{N/m}$, and natural frequency, $f = 21.7 \, \text{Hz}$, of the tube were measured experimentally. The initial transverse displacement of the tube was $x(0) = 2.5 \times 10^{-2} \, \text{m}$. The strain energy E_d lost in the first 1 s of free vibration (≈ 22 oscillations) with a damping ratio of 0.2% is:

$$E_d = \frac{1}{2} k_t (x(0))^2 - \frac{1}{2} k_t (x(1))^2 = \frac{1}{2} k_t (x(0))^2 (1 - (e^{-2\pi.21.7.0.002})^2), \quad E_d \approx 0.35 \, \text{J}. \tag{15}$$

Therefore, even if the total interfacial surface doubled within 1 s during the motion of the tube, it could only explain a 0.2% damping ratio. It will be seen in the next sections that a damping ratio of 0.2% is small compared to the overall two-phase damping. Therefore, even a maximum and extreme change of surface energy in a very short time would not be sufficient to explain the observed two-phase damping. Thus, surface energy variations in bubbly flow seem to play a minor role in two-phase flow damping.

Even during transition from bubbly to slug/churn flow, the surface energy drop may not exceed 0.4 J. Thus, dissipation of surface energy during the transition is not sufficient to explain two-phase flow damping. However, surface energy governs the flow pattern that may play a major role in two-phase damping. Consequently, another hypothesis is examined below to explain two-phase flow damping.

3.2. Two-phase viscous damping mechanism

The hypothesis that two-phase damping is a form of viscous damping in the liquid phase was first introduced by Carlucci and Brown (1983). Damping mechanisms and parameters have been reviewed by Hara (1993) and by Pettigrew and Taylor (2004). In this section, we shall show that this hypothesis is realistic, and that two-phase damping is related to the densities of each phase. Indeed, a transverse excitation of the tube induces a relative transverse velocity between the two phases, causing shear dissipation in the liquid. The mechanism can be considered as a coupled problem. Due to the oscillations of the tube, a forced excitation is generated on the gas phase through the liquid.

To illustrate the phenomenon, a simple model of a two-phase fluid inside a tube is shown in Fig. 3. In this model, the tube of radius R_o is allowed to move along the Y-axis. The gas phase is represented as a single, nondeformable gas cylinder of radius R_i, parallel to the tube axis and allowed to move along the X-axis only. Absolute coordinates X and Y are collinear. No axial flow or other axial phenomena are considered; thus, the masses of liquid and gas are constant in an elemental length of the fluid filled tube. The two-dimensional equations of motion in the plane of the cross-section are

$$m_s \ddot{Y} + c_s \dot{Y} + k_s Y = F_s,$$ (16)

$$m_g \ddot{X} = F_g,$$ (17)

where m_g, m_s are the masses of the gas and tube elements; c_s and k_s are the equivalent damping coefficient and rigidity of the tube. The resulting forces F_s and F_g exerted by the liquid on the tube element and gas element will now be determined. The in-plane movement of the liquid is considered in the (r, θ)-coordinate system originating at the centre of the tube section. The tube is chosen as the reference frame. A two-dimensional approach is proposed where the velocity of the liquid inside the elementary control volume is written as $\vec{U} = u_r \vec{e}_r + u_\theta \vec{e}_\theta$. The liquid (water) is considered incompressible. The Navier–Stokes equations for the liquid phase include inertial terms due to the motion of the reference frame ($\rho_l \ddot{Y}$):

$$\frac{\partial u_r}{\partial r} + \frac{u_r}{r} - \frac{1}{r}\frac{\partial u_\theta}{\partial \theta} = 0,$$ (18a)

$$\frac{\partial u_r}{\partial t} + u_r \frac{\partial u_r}{\partial r} + \frac{u_\theta}{r}\frac{\partial u_r}{\partial \theta} - \frac{u_\theta^2}{r} = -\frac{1}{\rho_l}\frac{\partial P}{\partial r} + v_l \left(\frac{\partial^2 u_r}{\partial r^2} + \frac{1}{r^2}\frac{\partial^2 u_r}{\partial \theta^2} + \frac{1}{r}\frac{\partial u_r}{\partial r} - \frac{u_r}{r^2} - \frac{2}{r^2}\frac{\partial u_\theta}{\partial \theta} \right) + \ddot{Y} \cos(\theta),$$ (18b)

$$\frac{\partial u_\theta}{\partial t} + u_r \frac{\partial u_\theta}{\partial r} + \frac{u_\theta}{r}\frac{\partial u_\theta}{\partial \theta} - \frac{u_r u_\theta}{r} = -\frac{1}{\rho_l}\frac{1}{r}\frac{\partial P}{\partial \theta} + v_l \left(\frac{\partial^2 u_\theta}{\partial r^2} + \frac{1}{r^2}\frac{\partial^2 u_\theta}{\partial \theta^2} + \frac{1}{r}\frac{\partial u_\theta}{\partial r} - \frac{u_\theta}{r^2} + \frac{2}{r^2}\frac{\partial u_r}{\partial \theta} \right) - \ddot{Y} \sin(\theta).$$ (18c)

Momentum Eqs. (18b) and (18c) are combined using $(1/r)(\partial/\partial r)(r(c)) - (\partial/\partial\theta)((b))$ to give the vorticity equation

$$\frac{\partial \omega}{\partial t} + u_r \frac{\partial \omega}{\partial r} + \frac{u_\theta}{r}\frac{\partial \omega}{\partial \theta} + \omega \left(\frac{\partial u_r}{\partial r} + \frac{u_r}{r} + \frac{1}{r}\frac{\partial u_\theta}{\partial \theta} \right) = v_l \nabla^2 \omega,$$ (19)

where $\omega = (1/r)((\partial(r u_\theta)/\partial r) - (\partial u_r/\partial\theta))$ is the magnitude of the vorticity. Noting that the fourth term on the left-hand side is zero due to continuity, and by introducing the stream function

$$u_r = -\frac{1}{r}\frac{\partial \psi}{\partial \theta}, \quad u_\theta = \frac{\partial \psi}{\partial r}, \quad \|\nabla \times \vec{U}\| = \omega = \nabla^2 \psi,$$ (20)

the vorticity equations becomes

$$\frac{\partial(\nabla^2 \psi)}{\partial t} - \frac{1}{r}\frac{\partial \psi}{\partial \theta}\frac{\partial(\nabla^2 \psi)}{\partial r} + \frac{1}{r}\frac{\partial \psi}{\partial r}\frac{\partial(\nabla^2 \psi)}{\partial \theta} = v_l \nabla^4 \psi.$$ (21)

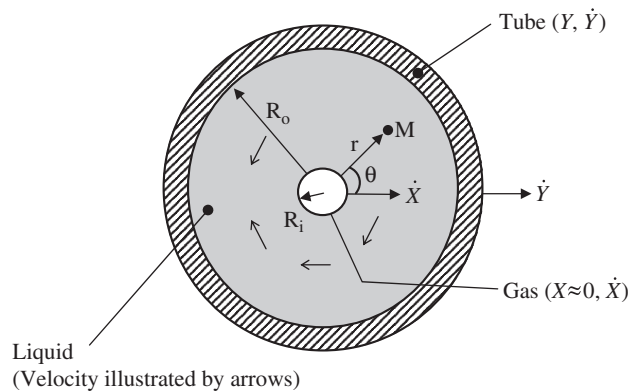Fig. 3. Cross section of a tube filled with liquid and a single cylindrical gas bubble. M is a point at coordinates (r, θ).

It is assumed that momentum is conserved in the in-plane direction perpendicular to the motion of the tube. It is also assumed that the motion of the gas phase is small compared to that of the liquid phase, with respect to the moving reference frame. Therefore,

$$\frac{\partial(\nabla^2\psi)}{\partial t} = \nu_l \nabla^4\psi. \tag{22}$$

This equation was previously obtained and solved by Chen (1987) for the case of an axially confined external flow. The only difference between Chen's formulation and the present formulation is the presence of the inertial forces due to the motion of the reference frame in Eqs. (18a) and (18c). Inertial forces are irrotational; their inclusion in the Navier–Stokes equations leads to the same vorticity equation as in Chen's work. However, the final expressions of forces F_g and F_s will be different for the two cases. Knowing that the position of the gas phase in the tube reference frame is X–Y, the above homogeneous equation allows the exact solution

$$\psi = (\dot{X} - \dot{Y})G(r)\sin(\theta),$$
$$G(r) = \frac{b_1}{r} + b_2 r + b_3 I_1(\lambda_0 r) + b_4 K_1(\lambda_0 r). \tag{23}$$

Therefore,

$$u_r = (\dot{Y} - \dot{X})\frac{G(r)}{r}\cos(\theta), \quad u_\theta = (\dot{X} - \dot{Y})G'(r)\sin(\theta), \tag{24}$$

where $\lambda_0^2 = i\Omega/\nu_l$, Ω is the complex frequency of the motion, and $G'(r) = dG/dr$. Integration constants b_i are dependent on the boundary conditions:

$$
\begin{array}{lll}
u_r(R_i,\theta) = (\dot{Y} - \dot{X})\cos(\theta) & \quad & G(R_i) = -R_i \\
u_r(R_0,\theta) = 0 & \quad & G(R_o) = 0 \\
u_\theta(R_i,\theta) = (\dot{X} - \dot{Y})\sin(\theta) & \Leftrightarrow & G'(R_i) = -1 \\
u_\theta(R_0,\theta) = 0 & \quad & G'(R_0) = 0.
\end{array}
\tag{25}
$$

The stress vector on the circumferential faces of a liquid element is

$$\vec{\sigma}(r) = \left(-P + 2\mu_l \frac{\partial u_r}{\partial r}\right)\vec{e}_r + \mu_l\left(r\frac{\partial(u_\theta/r)}{\partial r} + \frac{1}{r}\frac{\partial u_\theta}{\partial \theta}\right)\vec{e}_\theta. \tag{26}$$

The resulting forces on the gas cylinder (F_g) and on the tube (F_s) in the X direction are

$$F_g = \int \vec{\sigma}(R_i) \cdot \vec{e}_x r\, d\theta, \quad F_s = \int \vec{\sigma}(R_o) \cdot \vec{e}_x r\, d\theta. \tag{27}$$

Thus, the resulting force exerted in the X direction by an annular element of the liquid is

$$F_x(r) = \int_0^{2\pi}\left[\left(-P + 2\mu_l\frac{\partial u_r}{\partial r}\right)\cos(\theta) - \mu_l\left(r\frac{\partial(u_\theta/r)}{\partial r} + \frac{1}{r}\frac{\partial u_r}{\partial \theta}\right)\sin(\theta)\right]r\, d\theta. \tag{28}$$

Using Eqs. (25) and (28), the force exerted by the liquid on the gas cylinder (F_g) and on the tube (F_s) are obtained as follows:

$$F_g = \rho_l \pi R_i^2[(2b_2 + 3)\ddot{X} - (2b_2 + 2)\ddot{Y}] - 2\mu_l\pi(\dot{X} - \dot{Y}),$$
$$F_s = \rho_l \pi R_o^2[-2b_2\ddot{X} + (2b_2 - 1)\ddot{Y}]. \tag{29}$$

Finally, Eqs. (16) and (17) become

$$m_s\ddot{Y} + c_s\dot{Y} + k_s Y = \rho_l\pi R_o^2[-2b_2\ddot{X} + (2b_2 - 1)\ddot{Y}],$$
$$m_g\ddot{X} = \rho_l\pi R_i^2[(2b_2 + 3)\ddot{X} - (2b_2 + 2)\ddot{Y}] - 2\mu_l\pi(\dot{X} - \dot{Y}). \tag{30}$$

where

$$2b_2 = b_r - \frac{b_i}{i\Omega} \quad \text{with } (b_r, b_i) \in \Re^2,$$
$$2b_2\ddot{X} = b_r\ddot{X} + b_i\dot{X}. \tag{31}$$

The final equations of motion are

$$m_s\ddot{Y} + c_s\dot{Y} + k_sY = \rho_l\pi R_o^2[-b_r\ddot{X} + (b_r - 1)\ddot{Y} - b_i(\dot{X} - \dot{Y})],$$

$$m_g\ddot{X} = \rho_l\pi R_i^2\left[(b_r + 3)\ddot{X} - (b_r + 2)\ddot{Y} + \left(b_i - \frac{2v_l}{R_i^2}\right)(\dot{X} - \dot{Y})\right]. \tag{32}$$

If there is no relative displacement between the liquid and gas phases ($X = Y$), then

$$m_s\ddot{Y} + c_s\dot{Y} + k_sY = -\rho_l\pi R_o^2\ddot{Y},$$

$$m_g\ddot{Y} = \rho_l\pi R_i^2\ddot{Y}. \tag{33}$$

In this case, a nontrivial solution ($\ddot{Y} \neq 0$) is obviously not possible unless the mass of the gas phase (m_g) is $\rho_l\pi R_i^2$, which requires that $\rho_g = \rho_l$. This leads us to conclude that unless both phases have the same density, there exists a relative transverse displacement $Y-X \neq 0$ between the liquid and the gas phase. In addition, the relative transverse velocity between phases leads to two-phase damping through the terms $\rho_l\pi R_i^2(b_i - (2v_l/R_i^2))(\dot{X} - \dot{Y})$ and $\rho_l\pi R_o^2 b_i(\dot{X} - \dot{Y})$. This basic model shows that transverse motion of the tube comes with viscous dissipation due to the relative motion of the liquid and gas phases. This dissipation is the result of the difference in the densities of each phase. Moreover, it should be noted that a larger bubble yields a greater dissipation from the tube.

From a physical point of view, the foregoing results can be interpreted as follows. A transverse displacement of the tube causes a pressure differential in the liquid around the gas bubble, causing the bubble to move relative to the tube. The liquid thus circulates locally around the bubble, and viscous friction is initiated which causes damping in the fluid-structure system.

3.3. Relation between two-phase viscous damping and interface surface area

From the above simple model, it was shown that a force excitation is generated on the gas phase through the liquid. A more complete model would show that liquid flows around each bubble and induces forces that depend on the boundary conditions of the liquid ($X, Y, \dot{X}, \dot{Y}, \ddot{X}, \ddot{Y}, U_{2\varphi}$). The above simple model has yielded equations of the form (Eq. (32)):

$$m_s\ddot{Y} + c_s\dot{Y} + k_sY = m_{sg}\ddot{X} + m_{ss}\ddot{Y} + c_{sg}(\dot{X} - \dot{Y}),$$

$$m_g\ddot{X} = m_{gg}\ddot{X} + m_{gs}\ddot{Y} + c_{gs}(\dot{X} - \dot{Y}). \tag{34}$$

A more complete model could lead to

$$m_s\ddot{Y} + c_s\dot{Y} + k_sY = m_{sg}\ddot{X} + m_{ss}\ddot{Y} + c_{sg}(\dot{X} - \dot{Y}) + k_{sg}X + k_{ss}Y,$$

$$m_g\ddot{X} = m_{gg}\ddot{X} + m_{gs}\ddot{Y} + c_{gs}(\dot{X} - \dot{Y}) + k_{gg}X + k_{gs}Y. \tag{35}$$

The system is represented as a simple equivalent mechanism illustrated in Fig. 4, where the forces of the liquid on the gas are shown as spring and damper forces. These forces are calculated using a surface integral on the liquid/gas interface. As a result, the viscous damping ratio ζ is expected to be proportional to the interface surface area.

Finally, the gas is set in motion relative to the tube, due to these forces. Assuming that $\dot{X} = \lambda\dot{Y}$, where λ is probably related to the relative densities of the phases and the mixture velocity $U_{2\varphi}$, the energy dissipation in the liquid during one oscillation cycle is

$$E_{\text{damp}} = \int c(\dot{Y} - \dot{X})\,\mathrm{d}Y = \int c(1 - \lambda)\dot{Y}\,\mathrm{d}Y = \int c_{2\varphi}\dot{Y}\,\mathrm{d}Y. \tag{36}$$

The relative transverse velocity between phases is responsible for the viscous dissipation:

$$\zeta_{2\varphi} = g(S)f(U_{2\varphi}) = B_3 Sf(U_{2\varphi}), \tag{37}$$

where B_3 is a constant. The proportionality between two-phase damping and interface surface area comes from Gravelle et al.'s (2007) observations. It seems to be valid for bubbly flow only, whereas the damping mechanism may be different in other flow regimes. In the following sections, the relation was verified in bubbly flow through two simple experiments in which both the damping ratio and the interface surface area were measured precisely. Other parameters such as the bubble distribution pattern, bubble interaction and liquid turbulence may also play a major role in governing two-phase damping, but this study was focused on one parameter: the interface surface area.
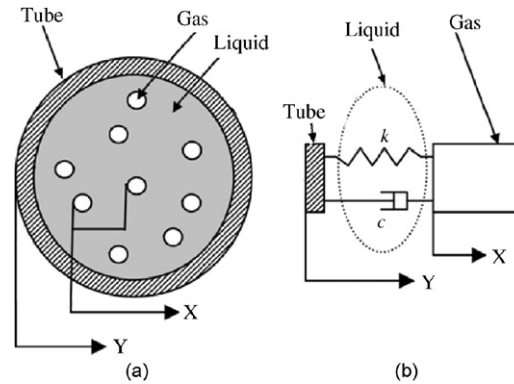
Fig. 4. Illustration of viscous damping mechanism in two-phase flow: (a) tube cross-section and (b) one degree of freedom model.

4. Evaluation of two-phase damping

Each experiment was performed on a vertical, clamped–clamped cylindrical tube. Three PVC tubes of similar effective lengths, but different internal diameters (21.2, 15.5 and 11.7 mm) were used. Test tube properties are given in Table 1.

The tubes were subjected to internal flows (described later), and were set to vibrate. The tubes were deflected with a transverse displacement of 10 mm at mid-length, and released using a quick-release device. The resulting transverse vibration was measured using strain gauges (Gravelle et al., 2007).

At first, damping was determined using both the logarithmic decrement and the random vibration techniques. Both methods were found to give the same results, as expected. Since it was faster and simpler, and because of suitable test conditions, the logarithmic decrement technique was then used for most tests.

5. Experiments with rigid spheres in water

5.1. Apparatus and procedure

This is one of two experiments used to verify the dependence of two-phase damping on the interface surface area. Small glass spheres of controlled diameter were let to settle in stagnant water. The glass spheres represent gas bubbles. The use of spheres to model bubbly flow is justified by the fact that, below a certain diameter near the capillary length (order of one mm), bubbles can be regarded as spheres. Bubble deformation can be ignored, because surface energy dissipation is negligible, as shown previously. Clearly, glass spheres do not coalesce, thus only bubbly flow can be simulated in this experiment. The two-phase flow has a very low homogeneous velocity. The low velocity of the spheres allows for a good visual observation of the flow.

The test rig shown in Fig. 5 consisted of six parts. Two funnels were laid out on top of each other, the lower funnel being directly attached to a vertical PVC tube. A tank, a filter and a plug were fitted at the bottom of the tube. The 21.2 mm diameter tube was supported by two clamps on a rigid wall. The glass spheres used had a diameter of 0.85 mm ± 0.1%. They were released from the top funnel to the lower one. The top funnel was not centred and the outlet diameter of the second funnel was identical to the diameter of the tube. Thus, the spheres spread evenly through the tube section. The spheres fell through the stagnant water in the tube, while damping measurements were performed. The spheres were stopped by the filter and collected inside the tank. At the end of each experiment, the plug was removed, the water was evacuated, and the spheres were retrieved from the tank.

Void fraction (the proportion of spheres in the water) was controlled by varying the outlet diameter of the top funnel. The interface surface area S was calculated using Eq. (6). The number of spheres N was determined as follows:

$$N = \frac{W_b}{\rho_b U_b ((\pi/6)d_b^3)}.$$
(38)

An empirical relation was developed to relate the granular mass flow rate W_b to the outlet diameter of the funnel. The mass of glass spheres flowing down the funnel in a given time was measured, and the mass flow rate was calculated. This was done for various funnel diameters, and the results are shown in Fig. 6.

Table 1
Characteristics of test tubes

Property	Tube #1	Tube #2	Tube #3
Length, L (m)	1.48	1.55	1.58
Inner diameter, D_i (mm)	21.2	15.5	11.7
Outer diameter, D_o (mm)	26.8	21.3	17.0
PVC Young's modulus E (GPa)	2.4	2.4	2.4
PVC density, ρ_s (kg/m³)	1380	1380	1380
Second moment of area of tube section I (m⁴)	1.54×10^{-8}	7.27×10^{-9}	3.18×10^{-9}
Tube mass, m (kg)	0.458	0.250	0.186
Theoretical frequency, f_n (Hz)	21.7	16.04	12.37
Structural damping, ζ_s (%)	0.7	0.65	0.6
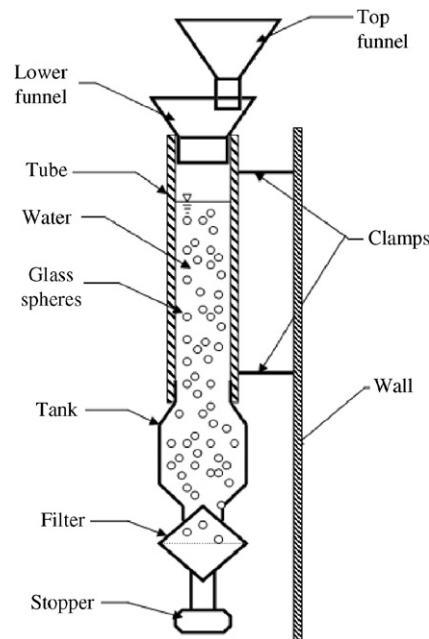
Fig. 5. Schematic representation of the test rig for glass–water experiments.

The mass density ρ_b of the spheres was also determined experimentally. A beaker partially filled with a given volume of water (V_1) was weighed, giving m_1. Glass spheres were then added, as in Fig. 7, and the resulting mass (m_2) and volume (V_2) were measured. The density of the glass spheres was then calculated:

$$\rho_b = \frac{m_2 - m_1}{V_2 - V_1}. \tag{39}$$

The sphere velocity U_b was determined by measuring the sedimentation time of glass spheres through a given length of water inside the tube. A few spheres were painted in red in order to be tracked easily. This was done for various funnel diameters, and results are given in Fig. 8. The velocities of a single unpainted and a single red sphere were compared to verify that the influence of paint is negligible. The single sphere velocity is approximately 0.07 m/s; it is shown as a straight horizontal line in Fig. 8, with dashed lines showing the error range.

Finally, the interface surface area S and void fraction ε were evaluated. Resulting values spread within $\pm 5\%$ around the average values, as shown in Fig. 9. When void fraction exceeded 35%, the glass spheres tended to cluster at the top of the water column. Thus, the experiments were limited to the following void fractions: 2%, 4%, 5%, 8%, 15%, 19%, 32% and 34% ($\varepsilon = 34\%$ requires a flow of 23,000 spheres per second).
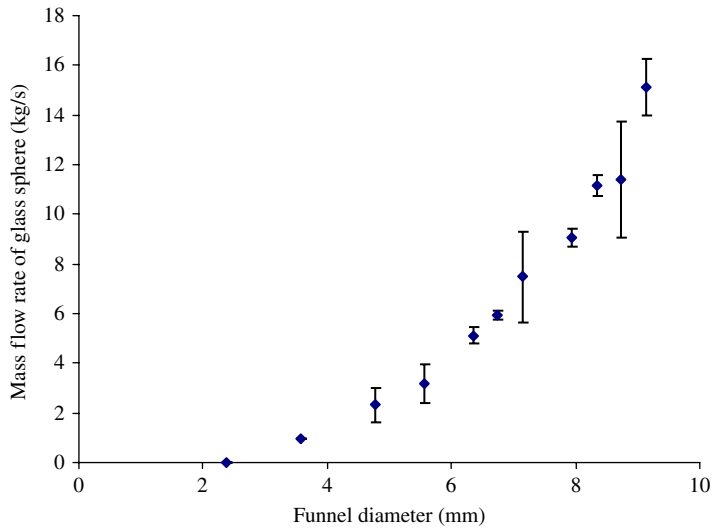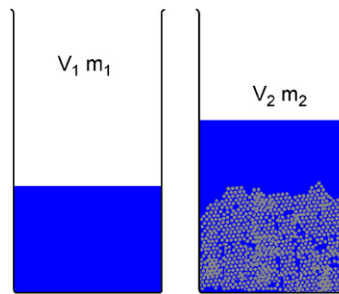
Fig. 6. Mass flow rate with respect to funnel diameter.

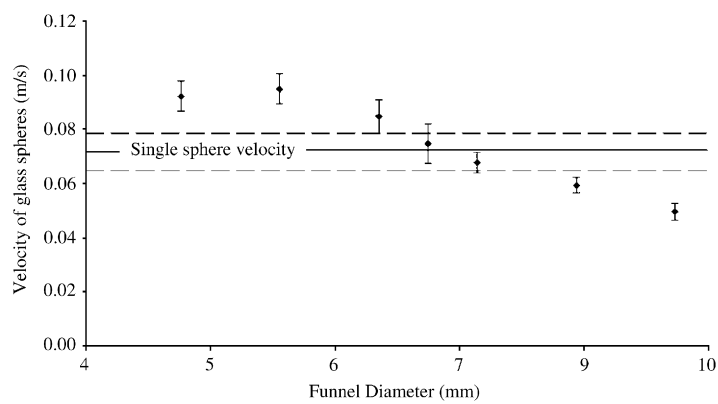Fig. 7. Empirical determination of glass spheres mass density ρ_b.

Fig. 8. Sedimentation velocity of glass spheres with respect to funnel diameter.

5.2. Results

For each void fraction, two-phase damping was measured three times. Fig. 10 shows that the results of the different tests are repeatable. For any given void fraction, the absolute empirical error of two-phase damping is less than 0.2%.
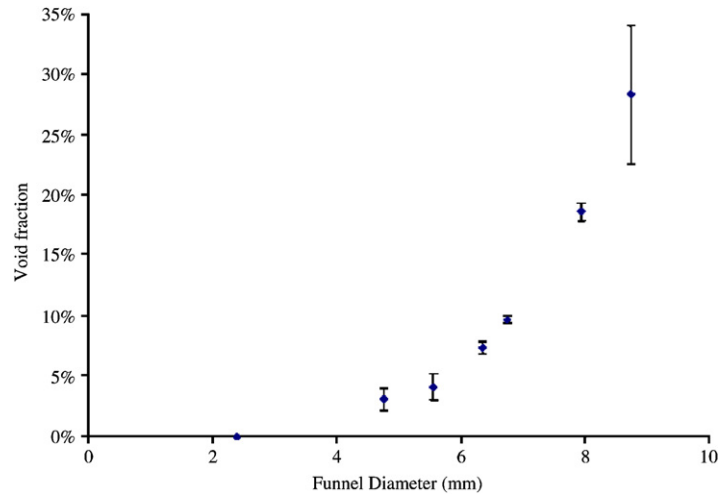
Fig. 9. Void fraction with respect to funnel diameter.
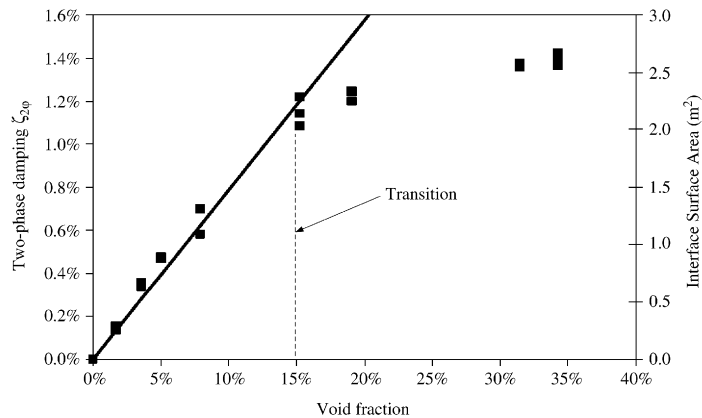
Fig. 10. Two-phase damping ratio in glass spheres–water mixture (■: two-phase damping; —: interface surface area).

The interface surface area was calculated as described above, and is represented by the straight full line. For void fractions up to 15%, two-phase damping is directly related to interfacial surface area. At 15%, a transition was observed in the behaviour of the glass spheres. The spheres started interacting with each other, due to their high concentration in the water. The motions of the spheres were no longer independent. Shear forces in the water were reduced, resulting in lower two-phase damping, as seen in Fig. 10. It should be noted from Figs. 8 and 9 that a 7 mm funnel diameter corresponds to both a void fraction of approximately 15% and a sphere velocity equal to that of a single sphere. For void fractions less than 15%, the sphere velocity is greater than the sedimentation velocity of a single sphere; for void fraction above 15%, the sphere velocity is lower than that of a single sphere. Two preliminary conclusions are put forward.

(i) First, the transition from bubbly flow to slug/churn flow was observed around $\varepsilon = 15\%$ in stagnant water. A strong interaction was detected between the glass spheres at void fractions above 15%. Spheres occupying more than 15% of the total volume attempt to group together and move slower than an isolated sphere. If such interaction existed between bubbles in air–water mixtures, it would lead to the coalescence of air bubbles.
(ii) Second, below $\varepsilon = 15\%$ ("bubbly" flow) the motions of glass spheres seem to be independent of each other. Therefore, the contribution of glass spheres (or bubbles) to the two-phase damping is linear with the number of spheres. Hence, two-phase damping may be directly related to the interface surface area.

6. Experiments with air in alcohol (static)

In the previous experiment, the correlation between two-phase damping and interface surface area was shown for void fractions up to 15% only. This second experiment is used to confirm that the interface surface area is a fundamental parameter in two-phase damping for all void fractions.

The experiment consists of creating a network of air bubbles at the bottom of the tube. Two-phase damping is measured while the bubbles rise to the surface of stagnant alcohol, the properties of which are given in Table 2. The number and size of the air bubbles are regulated. Homogeneity of the bubble flow is maintained, and so is the void fraction. Thus, the interface surface of the bubbles can be calculated and correlated with two-phase damping for all void fractions.

6.1. Apparatus and procedure

This experiment was carried out in the same clamped–clamped tube as in the previous experiment (21.2 mm diameter). An air injector is mounted at the bottom of the tube, and a reservoir is mounted at the top, as shown in Fig. 11.

The air injector is made of three parts, shown in an exploded view in Fig. 11. The main part is a perforated plate holding three needles of 10 mm length and 0.3 mm inside diameter. Premature coalescence of the bubbles close to the plate is avoided by placing the needles 10 mm apart, in a triangular pattern on the plate. The lower and upper parts of the air injector assembly are connected together to form two sealed chambers separated by the plate-and-needle unit. Air flows from the lower part to the upper part through the needles, and continues inside the tube.

The open reservoir at the top of the tube is used to contain any overflow of the alcohol–air mixture from the tube during the experiments. This happens for large void fractions.

A micro flow-meter is positioned upstream of the plate-and-needle unit to guarantee that the air flow is sufficiently low to prevent premature coalescence of the bubbles.

6.2. Bubble size

The diameter of the bubbles is predicted, in order to determine the appropriate needle hole. The following model is considered in Fig. 12, where the bubble reaches its full diameter d_b before it detaches from the needle. By isolating the bubble from its surrounding medium (alcohol) and by making a quasi-static assumption, the bubble is subjected exclusively to two forces: buoyancy (or Archimedes) force F_A and the capillary force F_γ, which retains the bubble to the needle:

$$F_\gamma = \gamma \pi D_h \cos(\theta) = \gamma \pi D_h \frac{D_h}{d_b}, \tag{40}$$

and

$$F_A = (\rho_l - \rho_g) g \frac{\pi}{6} d_b^3. \tag{41}$$

In the above equations, D_h is the diameter of the needle hole, and g is the gravitational acceleration. The bubble sets off when buoyancy overcomes the capillary force, yielding

$$d_b^4 = \frac{6 D_h^2 \gamma}{(\rho_l - \rho_g) g}. \tag{42}$$

Table 2
Properties of alcohol and water

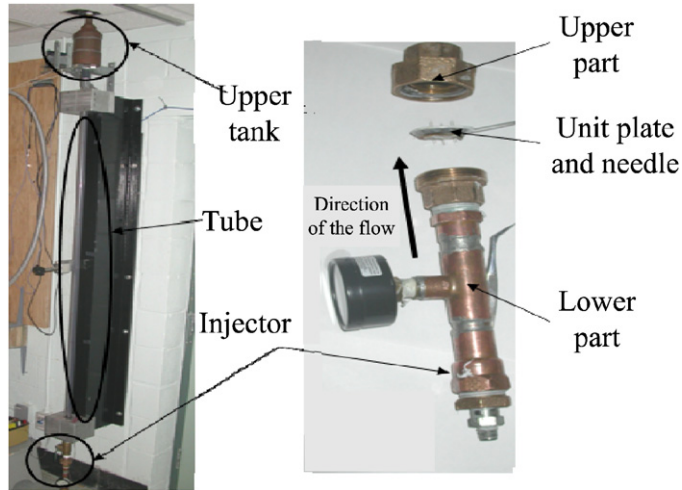| Property	Alcohol	Water
Temperature, T (°C)	20	20
Density of liquid, ρ_l (kg/m³)	860	1000
Density of the air, ρ_g (kg/m³)	1.18	1.18
Surface tension, γ (N/m)	0.022	0.074
Density ratio, ρ_l/ρ_g	728.8	847.5

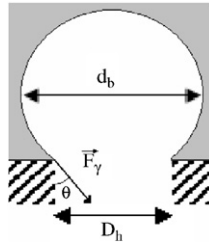Fig. 11. Photographs of the test rig for air–alcohol experiments.

Fig. 12. Model for air bubble.

The critical bubble diameter before coalescence is given by the maximum diameter for which a bubble can be regarded as a rigid sphere (Brodkey, 1967):

$$d_{\max}^2 = \frac{0.4\gamma}{(\rho_l - \rho_g)g}. \tag{43}$$

The combination of Eqs. (42) and (43) gives the diameter of the needle hole:

$$D_h^2 = \frac{0.4^2}{6} \frac{\gamma}{(\rho_l - \rho_g)g}. \tag{44}$$

Therefore, the critical bubble diameter is 1.7 mm in water and 1.0 mm in alcohol. The needle diameter that satisfies the critical bubble diameter is 0.26 mm for alcohol and 0.45 mm for water. The needles used have 0.3 mm internal diameter. The size of the bubbles produced during the experiments was measured, and the use of the 0.3 mm needles was validated. Both alcohol and water could be used, but it was observed that the air–liquid mixture is more homogeneous with alcohol, possibly because the needles provide closer bubble packing in alcohol.

During the experiments, the size of the bubbles was measured from photographs. Fig. 13 shows the measured bubble sizes with respect to void fraction. For all void fractions, the horizontal dimension (♦) is greater than the vertical dimension (■) of the bubbles. Except for a drop (which is significant on the horizontal dimension) near a 15% void fraction, both dimensions are relatively constant. Void fraction was determined from the difference between the mixture level inside the tube during the injection and the liquid level prior to the injection. As shown in Fig. 14, void fraction is fairly linear with gas flow rate, and resulting values spread within ±5% around the average values. The mean values were used to calculate the interface surface area in the mixture.

6.3. Results

Two-phase damping was measured twice for various void fractions ranging from 3% to 33%. The data points are given in Fig. 15, showing that the tests are repeatable.

The trend through the data points is shown as a thick line, and the interface surface area is shown as a thin line (×). For bubbly flow (low void fractions), the interface surface area is calculated using Eq. (8), and considering each bubble as an ellipsoid. The interface surface area in slug/churn flow was evaluated from the following model:

$$S = S_{\text{bubbles}} + S_{\text{slugs}} = 2\pi N' \left(a^2 + b^2 \frac{e}{\tan e} \right) + N_{\text{slug}}(2\pi D_i^2 + \pi D_i L_{\text{slug}}), \tag{45}$$

where a and b are the minor and major axes of the ellipsoid and $e = \arcos(a/b)$; N_{slug} is the number of slugs in the tube, and L_{slug} is the average slug length, as shown in Fig. 16. The number of bubbles N' is calculated using Eq. (7) and considering bubbly flow between slugs. Fig. 17 shows the ratio of slug length to tube length with respect to void fraction. The error bars do not correspond to measurement error which is very low but to the heterogeneity of bubble size. We can see that this heterogeneity is relatively small. The number of bubbles in Eq. (45) is

$$N' = \frac{\varepsilon' \pi (D_i/2)^2 (L_b/L_{\text{slug}})L}{V_b}, \tag{46}$$
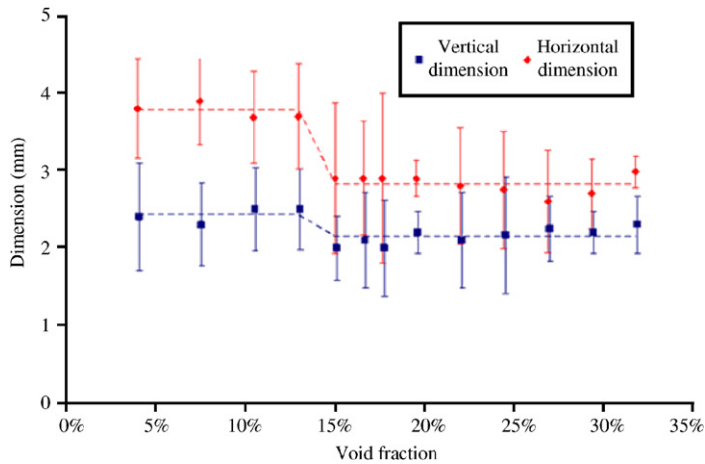
Fig. 13. Bubble dimensions with respect to void fraction in air–stagnant alcohol (■: vertical dimension; ♦: horizontal dimension).
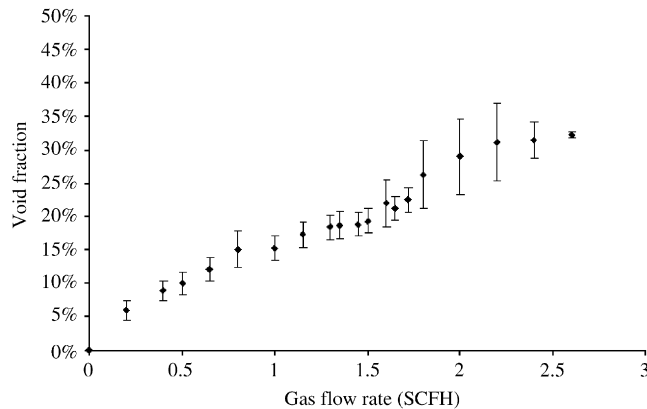
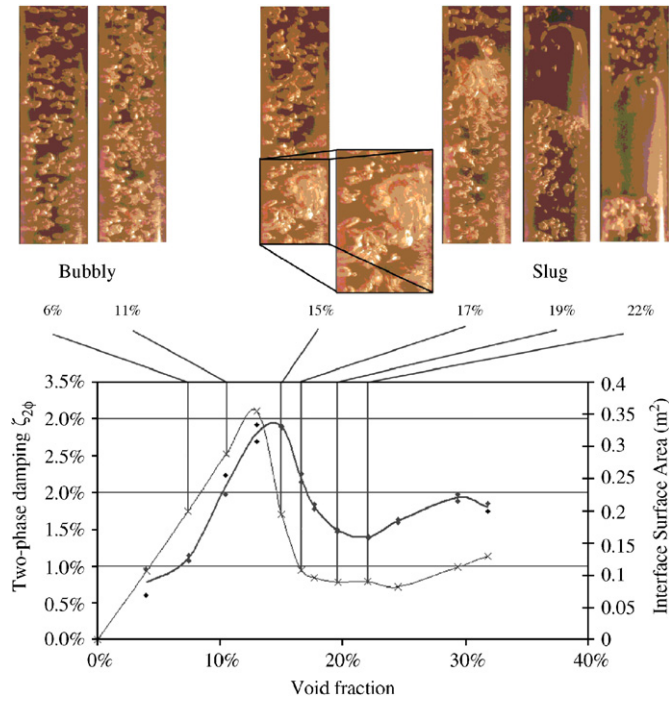Fig. 14. Void fraction in air–stagnant alcohol with respect to gas volume flow rate.

Fig. 15. Damping ratio and interface surface area in air–alcohol mixtures (♦: two-phase damping; ×: interface surface area).
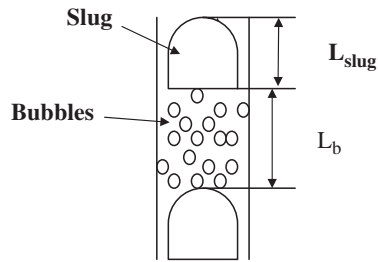

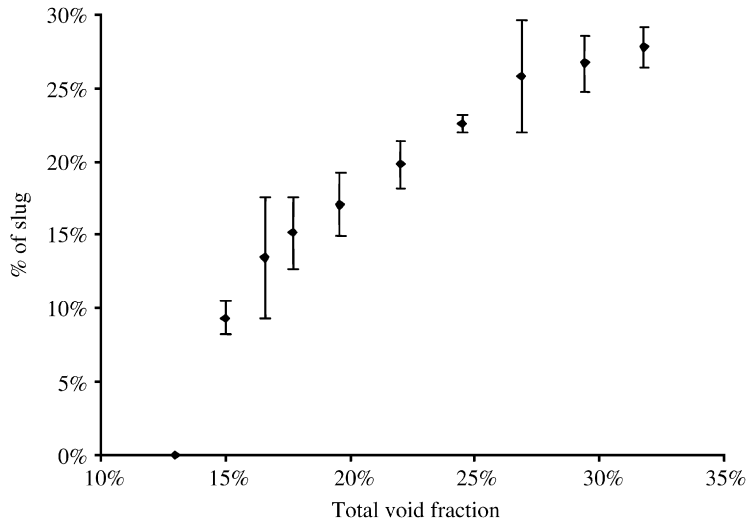Fig. 16. Illustration of slug flow.

Fig. 17. Relative slug length with respect to total void fraction (100% is total tube length).

in which L_b/L_{slug} is the average length between each slug over the average length of slugs (see Fig. 16) measured from photographs. Fig. 17 shows the measured total length of slugs over the length of the picture that could be expressed as

$$\left(\frac{L_{slug}}{L_b + L_{slug}}\right) = \frac{1}{(L_b/L_{slug}) + 1}. \tag{47}$$

The bubble volume V_b is calculated from the measured horizontal and vertical dimensions of the bubbles, considering them as ellipsoids. We deduce ε' (void fraction between slugs) from the total void fraction and average lengths L_b and L_{slug}:

$$\varepsilon = \frac{V_b + V_{slug}}{V_t} = \frac{L_b \varepsilon' + L_{slug}}{L_b + L_{slug}}. \tag{48}$$

The photographs at the top of Fig. 15 were taken during the experiments. They clearly show that the flow is bubbly for void fractions up to 15%, and slug/churn for void fractions above 23%. According to the photographs, the bubbles begin to interact at a void fraction of approximately 15%, which would mark the beginning of the transition from bubbly flow to slug/churn flow. A close-up of the photo at 15% void fraction was added to show this interaction clearly.

As in the previous experiment, there is a remarkably good correlation between the interface surface area and the two-phase damping ratio. However, the relationship between the two parameters is somewhat different below and above $\varepsilon = 15\%$. The constant of proportionality that relates the two-phase damping ratio to the interface surface area is higher in slug/churn flow ($\varepsilon > 15\%$) than it is in bubbly flow ($\varepsilon < 15\%$). Apparently, there is an additional damping mechanism in slug/churn flow, which is also related to the interface surface area. It is possible that considerable energy dissipation occurs in the wake of the slugs, which are moving transversally due to the motion of the tube.

7. Discussion

The two experiments described above show that two-phase damping is directly proportional to the interface surface area. The constant of proportionality is different for bubbly flow than for slug/churn flow.

Also, in the air–alcohol mixture, the damping ratio increases quasi-linearly with void fraction in bubbly flow. Both the damping ratio and the interface surface area fall abruptly when the void fraction reaches the transition point from bubbly to slug/churn flow. If this trend also exists in other two-phase flows, measuring the damping ratio could be used as a technique for detecting this transition. Experiments were also performed on tubes subjected to internal air–water two-phase flows, as described later.

In stagnant liquid ($u_{gs} \ll 1$), both experiments show that the transition from bubbly to slug/churn flow occurs near 15% void fraction. Experimental observations suggest that the transition from bubbly to slug/churn flow is related to the confinement of gas bubbles. When the distance between bubbles (or spheres) is too small, they start interacting. In the case of rigid spheres, the spheres and the liquid between them move together. As a result, less viscous friction occurs and less energy is dissipated than if the spheres moved independently. In the case of gas bubbles, the interaction leads to coalescence and lower energy dissipation.

Although the diameter is not the same for glass spheres (0.85 mm) and bubbles (1.0 mm), the transition occurs at almost the same void fraction in both cases (around $\varepsilon = 15\%$). The distance between spheres (or bubbles) was calculated assuming homogeneous packing of the gas phase, in order to determine its relationship with the transition void fraction.

We use the following notation: l is the distance between spheres and d is the sphere diameter (the centre-to-centre distance between the spheres is $l + d$). Different hypotheses can be made concerning the arrangement of the spheres in the flow. A cubic arrangement, a triangular prism arrangement and a pyramidal lattice arrangement are considered.

7.1. Cubic arrangement

A cubic arrangement is shown in Fig. 18. Each cube is delimited by eight bubbles; one-eighth of each bubble is contained in each cube. The void fraction in one cube is calculated as the volume ratio of the gas phase over the total volume:

$$\varepsilon = \frac{8 \times (1/8) \times V_{sphere}}{V_{cube}} = \frac{8 \times (1/8) \times (\pi/6)d^3}{(l + d)^3}. \tag{49}$$

Consequently, the ratio of the distance between bubbles to the bubble diameter is

$$\frac{l}{d} = \left(\frac{\pi}{6\varepsilon}\right)^{1/3} - 1.$$

(50)

7.2. Triangular prism arrangement

A triangular prism arrangement is shown in Fig. 19. The height (x) and area (A) of an equilateral triangle of length ($l+d$) are

$$x^2 + \left(\frac{l+d}{2}\right)^2 = (l+d)^2, \quad x = \frac{\sqrt{3}}{2}(l+d)$$

(51)

and

$$A = \frac{x(l+d)}{2} = \frac{\sqrt{3}}{4}(l+d)^2.$$

(52)

Each prism is delimited by six bubbles; one-twelfth of each bubble in contained in each prism. The void fraction in one prism is

$$\varepsilon = \frac{6 \times (1/12) \times V_{\text{sphere}}}{V_{\text{prism}}} = \frac{6 \times (1/12) \times (\pi/6)d^3}{(\sqrt{3}/4)(l+d)^3}.$$

(53)

Consequently, the ratio of the distance between bubbles to the bubble diameter is

$$\frac{l}{d} = \left(\frac{\pi}{3\varepsilon\sqrt{3}}\right)^{1/3} - 1.$$

(54)
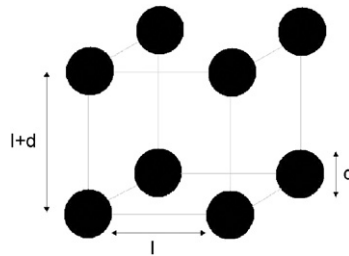
Fig. 18. Cubic bubble arrangement.
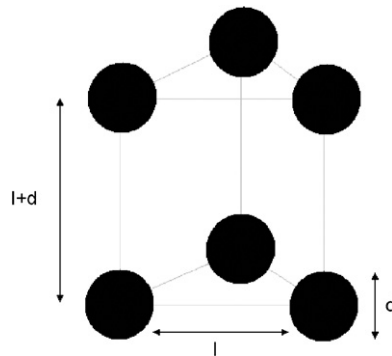
Fig. 19. Triangular prism bubble arrangement.

7.3. Pyramidal arrangement

A pyramidal arrangement is shown in Fig. 20. This is the most compact arrangement that can be achieved. Simple calculations can be carried out by using a hexagonal prism pattern. The height of one prism is $2z$, with z being the height of one triangular pyramid;

$$z^2 + \left(\frac{2}{3}x\right)^2 = (l+d)^2, \quad z = \frac{\sqrt{6}}{3}(l+d). \tag{55}$$

The area of the equilateral triangle at the base of each pyramid is A, calculated as in Section 7.2. The base of one prism is composed of the bases of six pyramids, so the volume of the prism is

$$V_{\text{total}} = 6A \times 2z = 6\frac{\sqrt{3}}{4}\frac{2\sqrt{6}}{3}(l+d)^3 = 3\sqrt{2}(l+d)^3. \tag{56}$$

Each prism is delimited by 12 bubbles; one-sixth of these bubbles in contained in each cube. In addition, the prism contains two half-bubbles (one at the top and one at the bottom of the prism) and three complete bubbles inside the prism. The void fraction in one prism is

$$\varepsilon = \frac{(12 \times (1/6) + 2 \times (1/2) + 3) \times V_{\text{sphere}}}{V_{\text{phexa}}} = \frac{6 \times (\pi/d)d^3}{3\sqrt{2}(l+d)^3}, \quad \frac{3\sqrt{2}}{\pi}\varepsilon = \frac{1}{(1+(l/d))^3}. \tag{57,58}$$

Consequently, the ratio of the distance between bubbles to the bubble diameter is

$$\frac{l}{d} = \left(\frac{\pi}{3\varepsilon\sqrt{2}}\right)^{1/3} - 1. \tag{59}$$

7.4. Transition void fraction

The general expression for any of the above arrangements can be expressed as

$$\frac{l}{d} = B\left(\frac{1}{\varepsilon}\right)^{1/3} - 1, \tag{60}$$

where constant B depends on the arrangement. Fig. 21 shows the evolution of ratio l/d with respect to void fraction, for each of the three arrangements. It can be seen that ratio l/d depends largely on void fraction, and not so much on the selected arrangement. Finally, assuming the transition occurs at void fraction $\varepsilon = 15\%$, the ratio of the distance
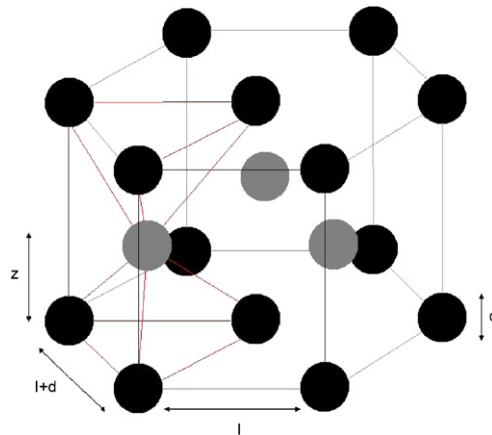

Fig. 20. Pyramidal bubble arrangement (the most compact arrangement).

between bubbles to the bubble diameter at transition would be:

$\dfrac{l}{d} \approx 0.52$ for the cubic lattice,

$\dfrac{l}{d} \approx 0.59$ for the triangular prism lattice,

$\dfrac{l}{d} \approx 0.7$ for the pyramidal lattice.

In the most general case,

$$\varepsilon = B^3 \frac{\langle d^3 \rangle}{(\langle l \rangle + \langle d \rangle)^3}. \tag{61}$$

From this calculation, it can be concluded that, at 15% void fraction, the typical distance between bubbles is somewhere between one bubble radius and one bubble diameter. Krishna and van Baten (1999) have shown from simulations that air bubbles having a diameter less than 9 mm rise in water with a transverse oscillatory motion (Fig. 22). The typical amplitude of this oscillation is in the order of one bubble radius to one bubble diameter. This oscillatory motion could induce lateral contact between bubbles, and could possibly explain the occurrence of a transition between bubbles and slug flow in stagnant liquid where turbulence is minimal.

8. Experiment with air–water two-phase flow

8.1. Apparatus and procedure

In this experiment, water and air are supplied at normal ambient pressure and temperature. Damping measurements are performed while the pre-measured mixture is injected at the bottom of the vertical tube, as shown in Fig. 23.
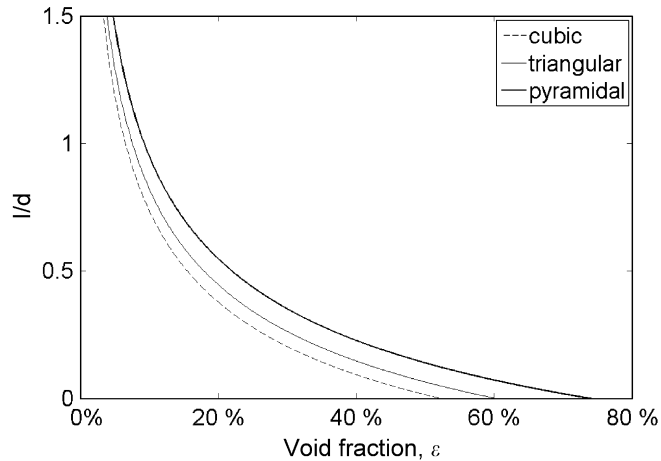

Fig. 21. Bubble distance to diameter ratio (*l/d*) with respect to void fraction for various bubble arrangements.
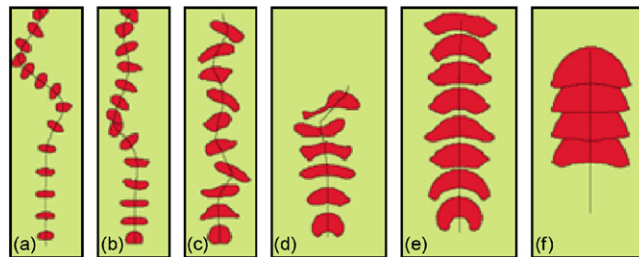

Fig. 22. Two-dimensional simulations of the rise trajectories of air bubbles in water (Krishna and van Baten, 1999). The bubble sizes are: (a) 4 mm, (b) 5 mm, (c) 7 mm, (d) 9 mm, (e) 12 mm, and (f) 20 mm.

The tests have two purposes. One is to establish the behaviour of two-phase damping with respect to the internal diameter of the tube, and to confirm the effect of confinement on bubble coalescence. The second purpose is to confirm the validity of the method suggested above, by which flow regime transitions could be detected from damping measurements.

The tests were carried out on all three PVC tubes (Table 1), for volumetric quality β ranging from 0% to 90%. For simplicity and consistency, flow conditions are given in terms of the homogeneous parameter. Homogeneous flow velocities ranged from 1 to 5 m/s for the 21.2 mm tube, from 1 to 9 m/s for the 15.5 mm tube and from 2 to 11 m/s for the 11.7 mm tube. A full description of the test loop is given in Gravelle et al. (2007). For each test configuration, photographs were taken to determine the flow regime and possible bubble interactions.

9. Results and discussion

9.1. Effect of void fraction

The measurement results are presented in Figs. 24–26 for the 21.2 mm, the 15.5 and 11.7 mm diameter tubes. Once again, the distinctive behaviour of two-phase damping with void fraction can be observed. For each tube and flow velocity, damping increases gradually, reaches a maximum, and decreases thereafter as void fraction increases. This is in agreement with previous studies on two-phase damping (Carlucci, 1980). Two-phase damping $\zeta_{2\varphi}$ evolves quasi-linearly with void fraction from 0% up to a critical value of ε in conformity with Eq. (37). The critical void fraction corresponds to the transition between bubbly and slug/churn flow, and increases with homogeneous flow velocity. It seems that the proportionality between the interface surface area and two-phase damping ratio is valid for bubbly two-phase flows. For void fractions beyond the critical value, two-phase damping decreases, and is no longer proportional to void fraction. The sudden change of behaviour seems to result from a transition in flow regime.

9.2. Effect of tube diameter

In bubbly flow, bubbles are considered spherical. For a given void fraction, the number of bubbles, thus the interface surface area, increases with tube diameter. However, the size of the bubbles also increases with the tube diameter, thus contributing to a smaller interface surface area. According to Eq. (14), the combined effects of the number and size of
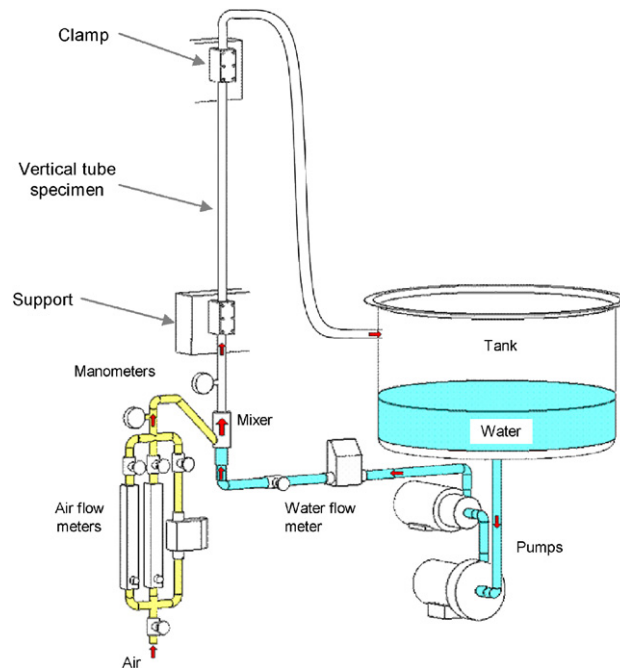

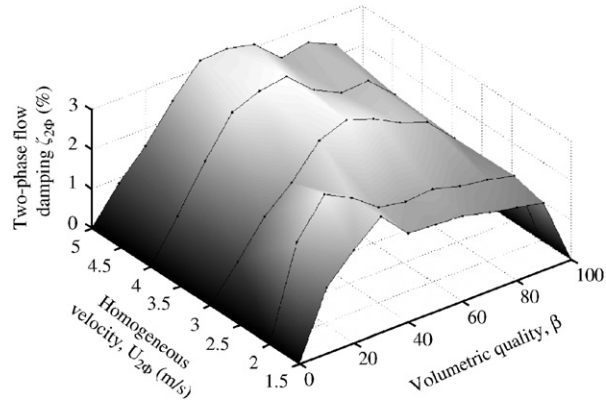
Fig. 23. Test loop for two-phase flow experiments.

Fig. 24. Behaviour of the two-phase damping ratio versus volumetric quality and homogeneous velocity, $D_i = 21.2$ mm.
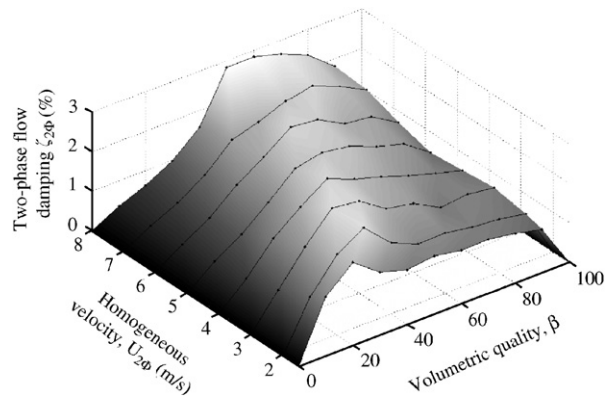

Fig. 25. Behaviour of the two-phase damping ratio versus volumetric quality and homogeneous velocity, $D_i = 15.5$ mm.
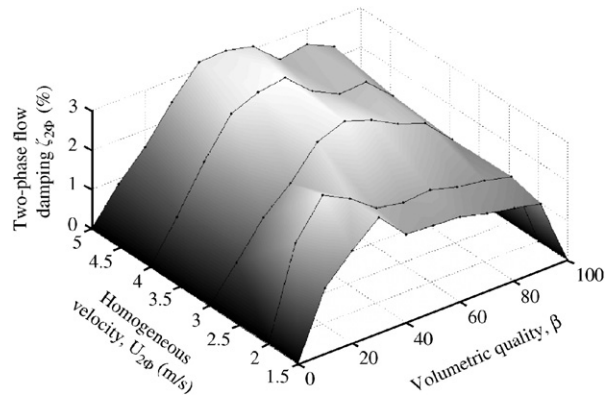

Fig. 26. Behaviour of the two-phase damping ratio versus volumetric quality and homogeneous velocity, $D_i = 11.7$ mm.

the bubbles is that interface surface area increases with the tube diameter: $S \propto D^{1.52}$. Hence, a greater damping ratio is expected in larger tubes.

The tube diameters given in Table 1 are sufficiently different to provide a good experimental assessment of the influence of tube diameter on two-phase damping. The results are compared for the different diameters in
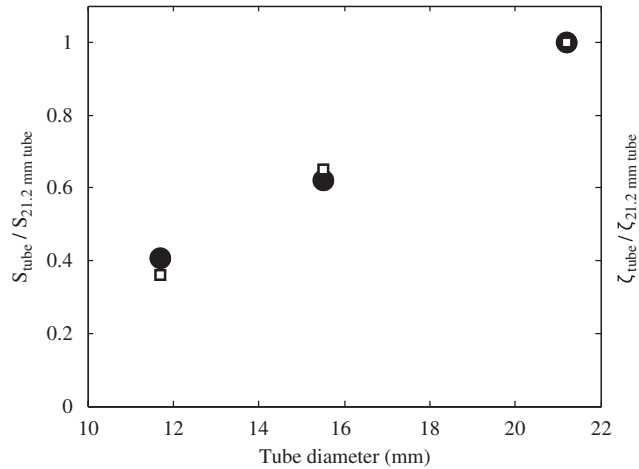
Fig. 27. Comparison of interface surface area and two-phase damping with respect to tube diameter (■: ratio of interface surface area; ●: ratio of damping values).
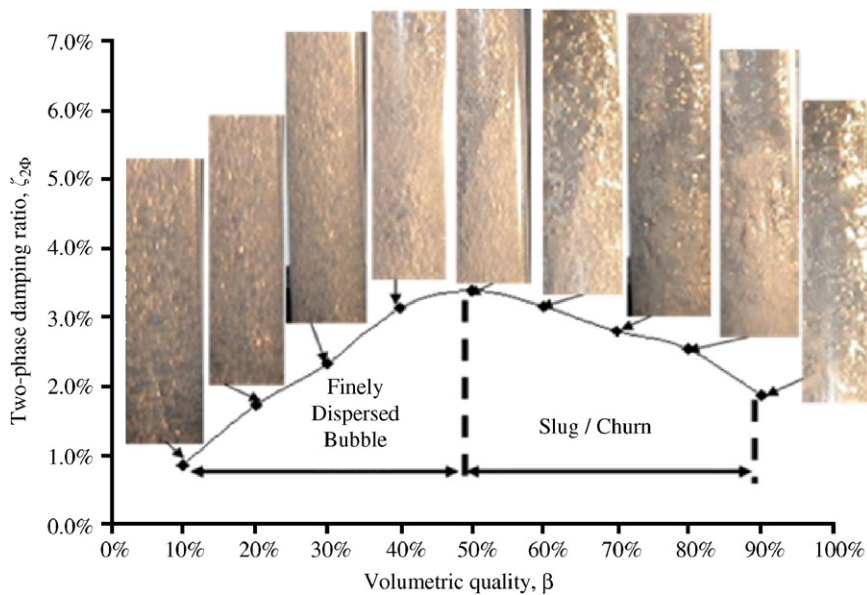

Fig. 28. Correlation between two-phase damping ratio and flow pattern, $D_i = 21.2$ mm (3 m/s).

Figs. 24–26. All three plots show a similar pattern: the critical void fraction (where maximum damping is observed) increases with flow velocity. Thus, the qualitative damping behaviour does not depend on tube diameter.

However, all damping values decrease for smaller diameter tubes, as shown in Figs. 24–26. This is observed not only in bubbly flow but also in slug flow. Using the average two-phase damping values for each tube in bubbly flow, we have compared the evolution of damping with that of interface surface area ($S \propto D^{1.52}$), relative to the tube diameter. The diameter ratio between the 11.7 and 21.2 mm tubes is 55%, and the interface surface area for the 11.7 mm tube is estimated at 40% that for the largest tube. For the 15.5 mm tube, the diameter ratio is 73%, and the estimated interface surface area ratio is 62%. For the 21.1 mm tube, both the diameter ratio and the interface surface area ratio are 100%. The ratios of interface surface areas are plotted in Fig. 27 with respect to tube diameter. Also reported in Fig. 27 are the ratios of damping values for the three tubes. The damping values for the 11.7 mm tubes are 36% of those for the 21.2 mm tube. For the 15.5 mm tube, damping values are 65% of those for the 21.2 mm tube. Therefore,

based on these tubes, the relationship between damping ratio and tube diameter is similar to the aforementioned relationship between interface surface area and tube diameter; thus, $\zeta \propto D_i^{1.52}$. Hence, it can be stated that the damping ratio is proportional to the interface surface area, and to the tube diameter, in the approximate proportion: $S \propto \zeta \propto D_i^{3/2}$.

The above experimental observations are valid only for bubbly flow. The influence of internal diameter D_i on two-phase damping is due essentially to the relationship between interface surface area and tube diameter. Actually, smaller tubes bring a greater confinement of the two-phase flow; the major impact is a smaller interface surface area, resulting in a lower damping ratio. Moreover, for a given homogeneous flow velocity, confinement in the two smaller tubes contributes to maintain a lower interface surface area. The results must therefore be examined in terms of flow regime.
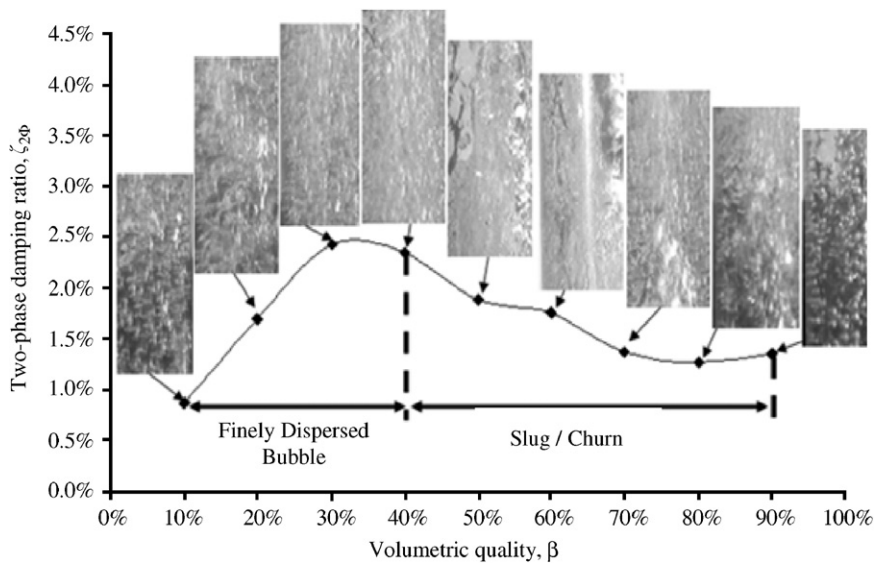

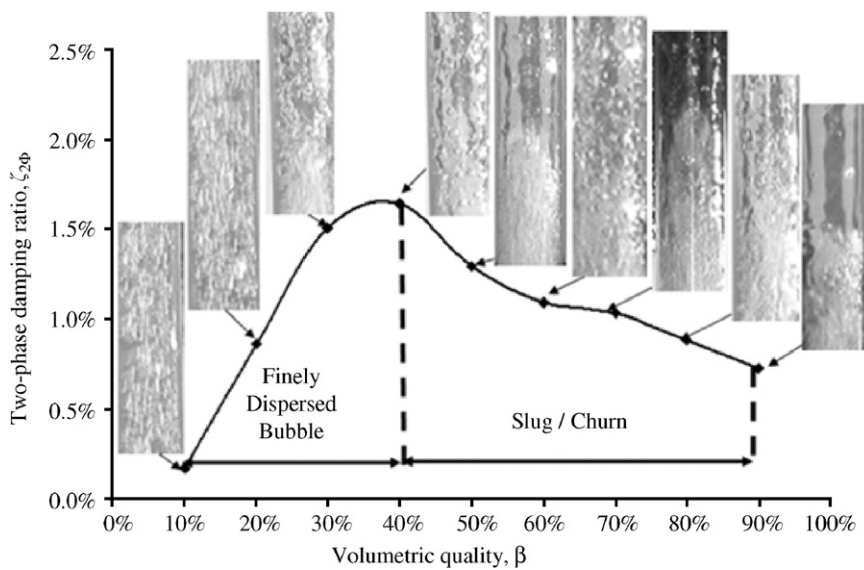Fig. 29. Correlation between two-phase damping ratio and flow pattern, $D_i = 15.5\,\text{mm}$ (3 m/s).

Fig. 30. Correlation between two-phase damping ratio and flow pattern, $D_i = 11.7\,\text{mm}$ (3 m/s).

9.3. Effect of flow regime

For each test configuration, photographs of the two-phase mixture were taken to determine the flow regime and possible bubble interactions. For each different tube and flow velocity, the photos show the behaviour of flow regime with void fraction, which is correlated with the behaviour of two-phase damping. Typical trends for each tube are presented in Figs. 28–30, for a flow velocity of 3 m/s. The flow regimes observed are identified on the figures.

In all test configurations, the flow regime varies from either bubbly or finely dispersed bubbles (at low void fractions) to slug/churn flow (at high void fractions). As mentioned previously, the shapes of the two-phase damping curves are reasonably similar. The damping values, however, are lower for smaller tubes.

In the bubbly flow regimes, two-phase damping increases almost linearly with void fraction, as mentioned before. Photographs clearly show that the overall number of bubbles becomes more significant and the bubbles become smaller as the void fraction and two-phase damping increase. This observation is useful to confirm the dependence of two-phase damping on the interface surface area.

In the slug/churn regime, damping decreases with a further increase in void fraction. Slugs contain large volumes of air for a small interface surface area. The number and the size of the slugs increase with void fraction, thereby reducing the interface surface area. Again, two-phase damping and interface surface area are correlated.

The maximum two-phase damping value observed for any given tube and flow velocity consistently occurs very close to the transition between bubbly flow and slug/churn flow. The maximum two-phase damping ζ_{max} and the flow regime transition occur at a lower void fraction for smaller tubes (around 50% for the 21.2 mm tube and around 25% for the two smaller tubes). Thus, the measurement of two-phase damping could very well be used for detecting the transition in air–water flow patterns. This conclusion will be confirmed using two-phase flow maps and pictures.

10. Conclusion

The purpose of this study was to understand the relation between two-phase damping, interface surface area and flow regime in internal two-phase flows in tubes. The results lead to the following conclusions.

 (i) Maximum two-phase damping consistently occurs at void fraction immediately below the transition from bubbly flow to slug/churn flow at a given flow velocity. It decreases rapidly for higher void fractions (as does the interface surface area). Thus, the transition could be detected from two-phase damping measurements.
 (ii) The transition from bubbly to slug flow was found near 15% void fraction in stagnant liquid, for two slightly different bubble sizes, for both air–alcohol and glass sphere–water mixtures. The ratio of the distance between bubbles with respect to the bubble diameter may be an important parameter for transition in stagnant liquid.
(iii) Two-phase damping is lower for smaller diameter tubes. Both the interface surface area and two-phase damping are proportional to $D_i^{3/2}$, where D_i is the internal tube diameter. Thus, two-phase damping is proportional to interface surface area between phases.
(iv) Two-phase damping is proportional to the interface surface area, both in bubbly and in slug/churn flows. However, the constant of proportionality is different in bubbly flow and slug/churn flow. Damping is higher in slug/churn flow than in bubbly flow for the same interface surface area. We presume that dissipation in the wake of the slug creates the additional damping.

References

Brodkey, R.S., 1967. The Phenomena of Fluid Motions. Addison-Wesley Press.
Carlucci, L.N., 1980. Damping and hydrodynamic mass of a cylinder in simulated two-phase flow. ASME Journal of Mechanical Design 102, 83–89.

Carlucci, L.N., Brown, J.D., 1983. Experimental studies of damping and hydrodynamic mass of a cylinder in confined two-phase flow. ASME Journal of Vibration, Acoustics, Stress, and Reliability in Design 105, 83–89.

Chen, S.S., 1987. Flow-induced Vibration of Cylindrical Structures. Hemisphere Publishing, New York, p. 30.

Collier, J.G., Thome, J.R., 1996. Convective Boiling and Condensation, third ed. Clarendon Press, Oxford University Press, p. 6.

Costigan, G., Whalley, P.B., 1997. Slug flow regime identification from dynamic void fraction measurements in vertical air–water flow. International Journal of Multiphase Flow 23 (2), 263–282.

De Langre, E., 2002. Fluides et solides. Edition de l'École Polytechnique, Paris.

Gravelle, A., Ross, A., Pettigrew, M.J., Mureithi, N.W., 2007. Damping of tubes due to internal two-phase flow. Journal of Fluids and Structures 23, 447–462.

Hara, F., 1993. Review of damping of two-phase flows. In: ASME, Pressure Vessels and Piping Division (Publication) PVP-Vol. 256; Pt. 2. Seismic Engineering, ASME, New York, pp. 87–101.

Hara, F., Kohgo, O., 1985. A theory for a vibrating circular rod damping in two-phase bubbly fluid. Transactions JSME 51, 143–148.

Hinze, J.O., 1955. Fundamentals of the hydrodynamic mechanism of splitting in dispersion process. AIChE Journal 1 (289).

Krishna, R., van Baten, J.M., 1999. Simulating the motion of gas bubbles in a liquid. Nature 398 (6724), 208.

Pettigrew, M.J., Taylor, C.E., 2004. Damping of heat exchanger tubes in two-phase flow: review and design guidelines. ASME Journal of Pressure Vessel Technology 126, 523–533.

Riverin, J.L., Pettigrew, M.J., 2004. Fluctuating forces in piping elements subjected to internal two-phase flow. In: Proceedings, 8th International Conference on Flow-Induced Vibrations. École Polytechnique, Paris, France, 5–9 July, vol. I, pp. 327–334.

Taitel, Y., Bornea, D., Duckler, A.E., 1980. Modeling flow pattern transitions for steady upward gas–liquid in vertical tubes. AIChE Journal 26 (3).

Wallis, G.B., 1969. One Dimensional Two-Phase Flow. McGraw-Hill, New York.